Cathode Surface-Induced, Solvation-Mediated, Micrometer-Sized Li_2O_2 Cycling for Li–O_2 Batteries

Ji-Jing Xu, Zhi-Wen Chang, Ying Wang, Da-Peng Liu, Yu Zhang, and Xin-Bo Zhang*

Rechargeable aprotic lithium–oxygen (Li–O_2) batteries have attracted intensive interest because of their high theoretical energy density (3600 Wh kg^{-1}), and they significantly outperform state-of-the-art Li-ion batteries and are a promising alternative to gasoline.[1–6] In a typical Li–O_2 battery, the electrochemical reaction pathway is $2Li^+ + 2e^- + O_2 \rightleftarrows Li_2O_2$, with the forward direction describing the cell discharge and the reverse direction describing charging.[7–10] Although the reaction is apparently simple, carrying out these processes rapidly, efficiently and sustainably for many cycles is a formidable challenge and is closely associated with parasitic chemistry/electrochemistry[11–14] and the specific growth and decomposition processes of the Li_2O_2 discharge products during battery cycling.[15–17]

Two different models for the Li_2O_2 growth mechanism have been proposed—the surface-adsorption pathway and the solvation-mediated pathway—and both are determined by the electron-donating propensity of the electrolyte solvent and the surface-binding energy on the cathode.[18–22] During battery discharge, O_2 undergoes a one-electron reduction to O_2^-. In the surface-adsorption pathway, the superoxide species (O_2^-* and/or LiO_2*, where * indicates surface-adsorbed O_2^- and LiO_2) adsorb on the cathode surface and undergo a second reduction, forming Li_2O_2 thin films (thickness < 10 nm) on the cathode surface,[18,19] severely passivating the cathode and limiting the maximum battery discharge capacity. In contrast, in the solvation-mediated pathway, the dissolved LiO_2(sol) and/or O_2^-(sol) undergo disproportionation, ultimately forming large Li_2O_2 toroidal crystals of variable size (typically less than 2 μm).[20–22] Fortunately, the formation of large Li_2O_2 toroids significantly improves the battery's capacity, rechargeability and cathode passivation.[23] To produce these toroidal crystals, several important authors, including Bruce,[24] Luntz,[23] Nazar,[25] and Shao-Horn,[26] have recently reported that the solvation-mediated pathway for Li_2O_2 growth can be significantly enhanced by employing high-donor-number solvents (electrolytes) with trace amounts of electrolyte additives (such as H_2O and CH_3OH) and/or a low current density. In comparison, the Li_2O_2 decomposition pathways during the recharge process have been much less studied. This pathway is generally understood to be initiated by a one-electron transfer process, forming surface-bound LiO_2* species.[27,28] If the LiO_2* undergoes a second oxidation on the cathode or Li_2O_2 surface to generate O_2, which is considered to be the most plausible route, the overall reactions are more commonly believed to consist of two-electron processes.[29] If the LiO_2(sol) diffuses in the solution and then is disproportionated to O_2, the overall decomposition would be a single-electron process expected to feature low overpotentials.[30,31] However, discussion of the enhanced solvation-mediated formation and decomposition process of Li_2O_2 by suppressing the cathode surface binding energy and its effect on battery performance have been rarely discussed. More importantly, most research efforts have been limited to exploring the Li_2O_2 growth mechanism in the first discharge/charge cycle only. Additionally, our understanding of the evolution mechanism of Li_2O_2 morphology and crystallinity over long-term cycling, which is vital for the development of long-life Li–O_2 batteries, is very limited.

Here, we demonstrate enhanced solvation-mediated growth/decomposition of the discharge product Li_2O_2 in Li–O_2 cells using a highly stable cathode based on herringbone-patterned carbon nanotubes (CNTs) coated with ruthenium(IV) oxide (RuO_2) nanoparticles (NPs). The RuO_2/CNT cathode exhibits a suppressed surface-binding energy toward the superoxide species (LiO_2 and O_2^-), thereby promoting the formation of LiO_2, with O_2^- readily diffusing to the electrolyte and rapidly forming/decomposing the micrometer-sized, flower-like Li_2O_2 assemblies reported here for the first time. We also reveal that this efficient formation/decomposition mechanism is sustainable over many cycles because of the minimal accumulation of side products on the RuO_2/CNT cathode and the presence of CO_2 in the electrolyte resulting from parasitic electrochemistry/chemistry during cycling. These factors endow the Li–O_2 battery with an ultrahigh specific capacity, relatively low overpotentials, and a long cycle life.

Figure 1a shows the synthesis strategy for the RuO_2/CNT cathode. We used a simple hydrothermal treatment to coat the herringbone CNT surface with ruthenium (IV) oxide (RuO_2) NPs, which deposit on the CNT defect sites to both passivate the defects on the CNT surface and enhance the electrocatalytic activity of the RuO_2/CNT composite. The transmission electron microscopy (TEM) and elemental mapping images indicate that the RuO_2 NPs only partially covered the CNT surfaces and were highly dispersed and uniform (Figure 1b,c

Dr. J.-J. Xu, Z.-W. Chang, Dr. Y. Wang, Prof. X.-B. Zhang
State Key Laboratory of Rare Earth Resource Utilization
Changchun Institute of Applied Chemistry
Chinese Academy of Sciences
Changchun 130022, P. R. China
Z.-W. Chang
University of Chinese Academy of Sciences
Beijing 100049, P. R. China
Dr. D.-P. Liu, Prof. Y. Zhang
Key Laboratory of Bio-Inspired Smart Interfacial Science and Technology of Ministry of Education
School of Chemistry and Environment
Beihang University
Beijing 100191, P. R. China
E-mail: jade@buaa.edu.cn

DOI: 10.1002/adma.201603454

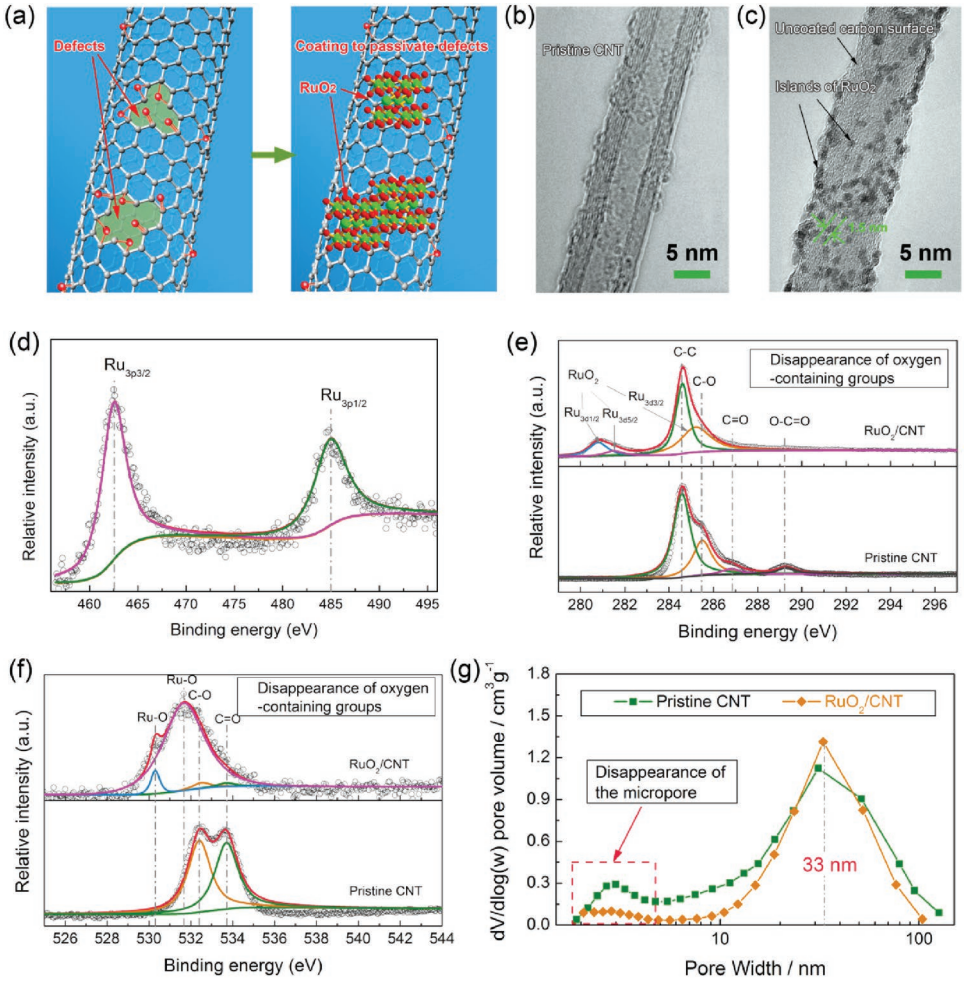

Figure 1. a) Schematic representations of the design and preparation of the RuO_2/CNT. b) TEM image of the pristine CNT. c) TEM image of the RuO_2/CNT. The surface of the CNT (light areas) is coated with well-dispersed RuO_2 islands with diameters of 1.5 nm (dark areas). d) Ru 3p XPS spectra of the RuO_2/CNT. e) C1s XPS spectra of the RuO_2/CNT. f) O1s XPS spectra of the RuO_2/CNT. The RuO_2 significantly decreases the number of defects on the CNT, as evidenced by the disappearance of peaks attributed to oxygen-containing groups (C=O, C—O, and O=C—O). g) The pore-size distributions of the pristine CNT and RuO_2/CNT. The tiny pores (3 nm) with ample oxygen-containing groups on the pristine CNT surface disappear on the RuO_2/CNT surface.

and Figure S1, Supporting Information). The average size of the RuO_2 NPs is ≈1.5 nm. Thermal gravimetric analysis (TGA) confirms a RuO_2 mass percent of 47% in the RuO_2/CNTs and the absence of both organic residues and water (Figure S2, Supporting Information). The partially covered CNT surface is characterized by islands of RuO_2 deposited on defect sites, leaving some of the CNT surface exposed. The CNT defect sites include, for example, C—O, C=O, and O—C=O groups, which have been found to be reactive toward the oxidation of ruthenium precursors.[32] X-ray photoelectron spectroscopy (XPS) was used to investigate the nature of the CNTs and RuO_2/CNT surface. The XPS peaks centered at 464.0 and 485.2 eV can be assigned to RuO_2 (Figure 1d). The C1s and O1s XPS spectra shown in Figure 1e,f indicate that the RuO_2 coating significantly decreases the amount of defects on the CNT, as evidenced by the disappearance of oxygen-containing groups' (C—O, C=O, and O—C=O) peaks. This result exactly agrees with the decreased I_D/I_G ratio resulting from the deposition of RuO_2 NPs (Figure S3, Supporting Information) and is further supported by pore-size distribution analyses of the CNTs and RuO_2/CNTs, which indicate fewer tiny holes (3 nm) with ample oxygen-containing groups on the RuO_2/CNT surface (Figure 1g). This RuO_2 coating prevents the decomposition of both the CNT surface and the ether (tetraglyme) solvent, which is a problem for Li–O_2 cells.[20,27,28] The electrochemical performance of RuO_2/CNT cathodes was then examined in Li–O_2 cells and compared to that of pristine CNT cathodes (i.e., RuO_2-free cathodes).

The role of the RuO_2/CNT cathode is demonstrated by the morphological and structural features of Li_2O_2 after discharge and recharge, after excluding the possible effects of the cathode morphology (Figure S4, Supporting Information). To shed light on the detailed Li_2O_2 growth process, field emission scanning electron microscopy (FESEM) was conducted at different galvanostatic discharge depths, a limited capacity of 2000 mAh g^{-1} and a current density of 200 mA g^{-1}

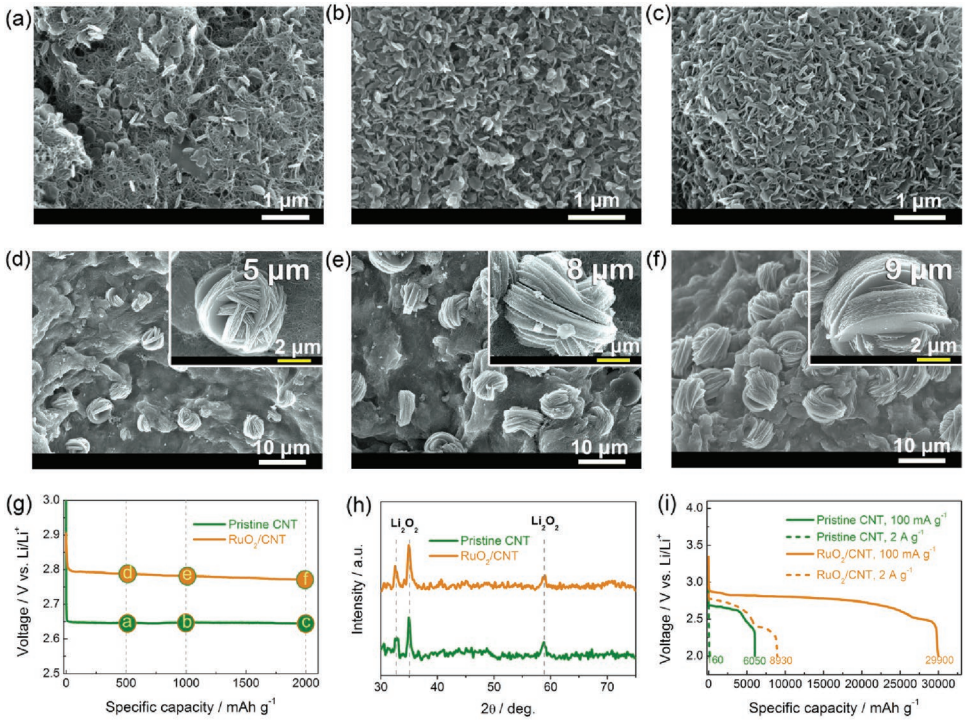

Figure 2. FESEM images of a) the discharged pristine CNT cathode at a current density of 200 mA g^{-1} and a specific capacity of 500 mAh g^{-1}, b) the CNT cathode at 1000 mAh g^{-1}, c) the CNT cathode at 2000 mAh g^{-1}, d) the discharged RuO_2/CNT cathode at 500 mAh g^{-1}, e) the discharged RuO_2/CNT cathode at 1000 mAh g^{-1}, and f) the discharged RuO_2/CNT cathode at 2000 mAh g^{-1}. Insets in (d–f) show the corresponding enlarged FESEM images. g) The discharge curves of Li–O_2 cells at a current density of 200 mA g^{-1} and a specific capacity limit of 2000 mAh g^{-1}. h) Corresponding PXRD patterns of the two types of discharged cathodes. The PXRD peaks can be assigned to Li_2O_2, although the morphology of the discharge product is different. i) The rate capability of the Li–O_2 cells with each type of cathode at current densities of 100 mA g^{-1} and 2 A g^{-1}.

(**Figure 2**). The FESEM image of the discharged CNT cathodes at the initial capacity of 500 mAh g^{-1} (point a in Figure 2g) reveals that the Li_2O_2 discharge product has a small disc/toroid (100–200 nm in size) morphology (Figure 2a), which is consistent with the results reported by other groups.[29–31,33] As the discharge capacity increases, more abundant discs/toroids are formed (Figure 2b,c). In sharp contrast, on the RuO_2/CNT cathodes at the initial 500 mAh g^{-1} capacity, micrometer-sized flower-like assemblies (5 μm in size) exist (Figure 2d), which have not been previously reported. As the capacity increases, increasing numbers of relatively large (9 μm) flower-like assemblies form (Figure 2e,f). Additionally, the flower-like assemblies on discharged RuO_2/CNT cathodes remain observable, even at a high discharge current density of 500 mA g^{-1}, whereas Li_2O_2 is only deposited as thin conformal films on the CNT cathode surface at this high current (Figure S5, Supporting Information), in general agreement with previous observations. The powder X-ray diffraction (PXRD) patterns of the discharged cathodes in Figure 2h confirm that in both cases, Li_2O_2 is the only crystalline discharge product, regardless of the morphological difference. The Li–O_2 cell with the RuO_2/CNT cathode exhibits an exceptionally high capacity of 29 900 mAh g^{-1} at a current density of 100 mA g^{-1}, which is more than five times the specific capacity of the cell with the pristine CNT cathode, i.e., 6050 mAh g^{-1} (Figure 2i). More importantly, a high capacity of 8930 mAh g^{-1} could be obtained even at a high current density of 2 A g^{-1}, which corresponds to superior rate performance. We argue that the improvement in capacity can be attributed to the formation of flower-like Li_2O_2 via the enhanced solvation-mediated mechanism (vide infra), which overcomes the charge-transport limitations inherent in the surface growth route and the electronically insulating property of Li_2O_2.[34]

Figure 3a schematically shows the two electrochemical (and/or chemical) Li_2O_2 growth pathways. In aprotic solvents, O_2 reduction initially proceeds through the one-electron reduction process to form LiO_2, which is present as both LiO_2 adsorbed on the electrode surface and LiO_2 dissolved in the electrolyte, according to the following equilibrium

$$LiO_2^{*} \rightleftharpoons Li^{+}(sol) + O_2^{-}(sol) + \text{ion pairs}\ (sol) + \text{clusters}\ (sol) \quad (1)$$

where * refers to surface-adsorbed species and (sol) indicates species in solution. The equilibrium is governed by the stability of the Li^+ and O_2^- ions in solution relative to that on the cathode surface, which is determined by two competing and crucial factors: the electron-donating propensity of the electrolyte solvent and the surface-binding energy on the cathode (Figure 3a). When the Gibbs free energy for LiO_2* on the cathode surface is lower than that for the dissolved species (Li^+(sol) + O_2^-(sol) + ion pairs(sol) + clusters(sol)) in the solvent, i.e., $\Delta G^\circ > 0$, the equilibrium lies to the left of Equation (1). The LiO_2* undergoes a second reduction, forming Li_2O_2 thin films (thickness < 10 nm) on the cathode surface through the surface-adsorption growth pathway

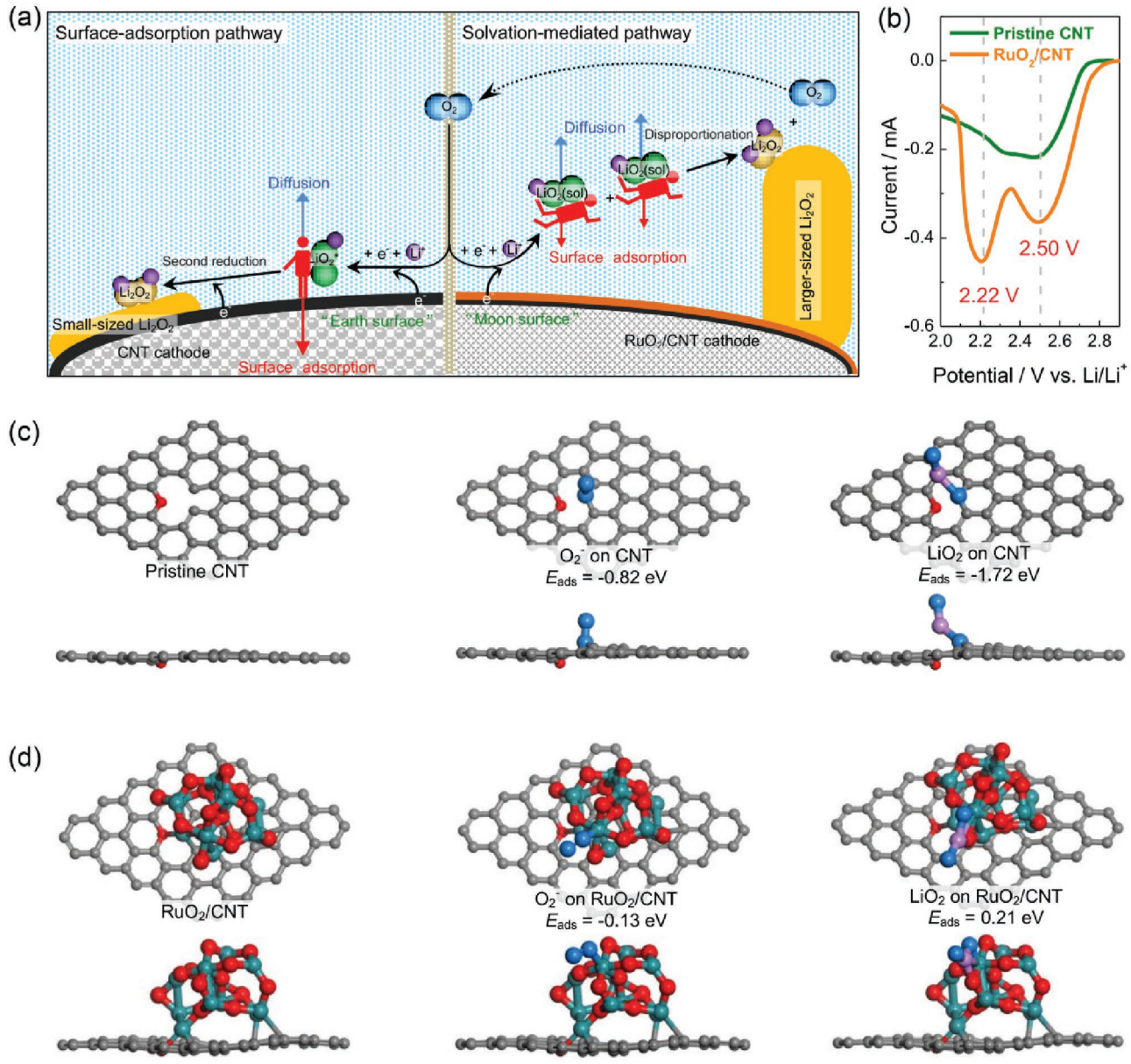

Figure 3. a) Schematic of the Li_2O_2 growth mechanism showing the surface-adsorption pathway follows when the Gibbs free energy for LiO_2* on the cathode surface exceeds that of the dissolved species and the solvation-mediated pathway follows when the dissolved species have lower Gibbs free energy than the LiO_2* on the surface. The RuO_2/CNT cathode possessing a suppressed surface binding energy toward the superoxide species is viewed as the "moon surface," and the CNT cathode is the "earth surface." b) LSVs performed at 0.05 mV s^{-1} with pristine CNT and RuO_2/CNT cathodes in Li–O_2 cells. The CNT cathode shows a single sharp peak in the LSV at ≈2.5 V, whereas the LSV curve for the RuO_2/CNT cathode exhibits a distinct second peak at ≈2.22 V. The first peak is attributed to surface-adsorption Li_2O_2 growth and the second peak is attributed to the solvation-mediated growth. c) Top and side views of optimized structures and the corresponding binding energies of O_2^- and LiO_2 on the double-defect CNT with a bound C—O—C group. d) The optimized structures and the corresponding binding energies of O_2^- and LiO_2 on the RuO_2/CNT coated with RuO_2. In each structure, the top and side views are shown in the upper and lower panels, respectively. Color code: carbon (gray), oxygen (red), ruthenium (dark green), lithium (pink), and oxygen atom of O_2^- and LiO_2 (blue).

$$LiO_2^* + e^- + Li^+(sol) \rightarrow Li_2O_2(s) \quad (2)$$

where (s) indicates a solid phase. In contrast, when the Gibbs free energy for the dissolved species is lower than that for LiO_2* on the surface, i.e., $\Delta G° < 0$, the equilibrium lies to the right, with the reduction proceeding predominantly along the solvation-mediated growth pathway:

$$Li^+(sol) + O_2^-(sol) + ion\,pairs(sol) + clusters(sol) \rightarrow Li_2O_2(s) + O_2(g) \quad (3)$$

where (g) indicates the gas state. The solubility of O_2^- in the electrolyte can activate a mechanism in which O_2^- acts as a redox mediator for the electrochemical growth of Li_2O_2 that is not limited by the charge transport of Li_2O_2 and results in

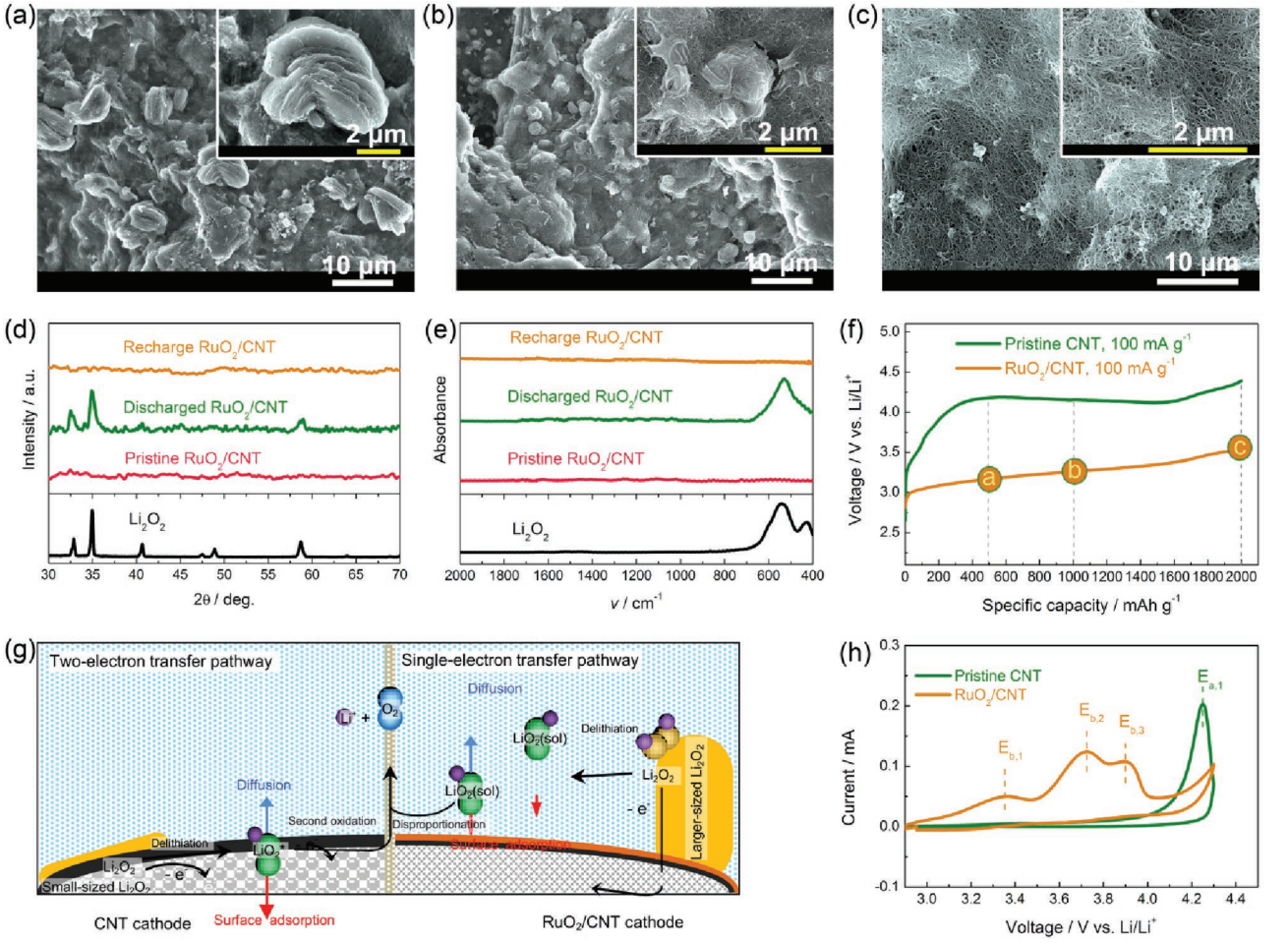

Figure 4. FESEM images of a) the recharged RuO_2/CNT cathode at a current density of 200 mA g^{-1} and a charge of 500 mA h g^{-1}, b) the RuO_2/CNT cathode recharged to 1000 mA h g^{-1}, and c) the RuO_2/CNT cathode recharged to 2000 mA h g^{-1}. d) XRD patterns and e) IR spectra comparing a pristine RuO_2/CNT cathode to cathodes at the end of discharge and charge at a specific capacity limit of 2000 mA h g^{-1}. The spectra for standard Li_2O_2 are also shown for reference. f) The recharge curves of Li–O_2 cells at a current density of 200 mA g^{-1} and a charge of 2000 mA h g^{-1}. g) Schematic of the Li_2O_2 oxidation mechanism showing the two-electron transfer pathway followed when LiO_2* is adsorbed to the cathode surface and the single-electron transfer pathway follows when LiO_2(sol) is dissolved in the electrolyte. h) CV of the discharged CNT cathode and the discharged RuO_2/CNT cathode in Li–O_2 cells at a constant scan rate of 0.1 mV s^{-1}.

large toroidal crystals (typically less than 2 μm in size at low current rates).[29–31,33] To understand the possible effect of the cathode surface properties on the Li_2O_2 growth pathway, density functional theory (DFT) calculations were performed using the Vienna ab initio simulation package. The optimized structures and the corresponding binding energies between the various reduced species (O_2^- and LiO_2 ion pairs) and both the CNT and RuO_2/CNT surfaces are shown in Figure 3c,d. We find that the binding energies of the reduced species on CNT surface (–0.82 eV for O_2^- and –1.72 eV for LiO_2) are much higher than those on the RuO_2/CNT surface (–0.13 eV for O_2^- and 0.21 eV for LiO_2), indicating that the "agravic" species are more easily liberated from the RuO_2/CNT surface and that they spread to the electrolyte. Therefore, the solvation-mediated growth pathway is believed to produce relatively large Li_2O_2 (Figure 3a), in good agreement with the experimental observations (Figure 2). This is further supported by the discharge linear scan voltammograms (LSVs) of the Li–O_2 cell with both CNT and RuO_2/CNT cathodes (Figure 3b). Other authors have recently suggested that the first peak (at ≈2.5 V) in the LSV is related to the surface-adsorption growth pathway of Li_2O_2 and that the second peak (at ≈2.3 V) is related to the solvation-mediated growth pathway of Li_2O_2, where O_2^- acts as a redox mediator.[21,23] The LSV of cells with the RuO_2/CNT cathode also exhibits a strong second peak ascribed to the solvation-mediated Li_2O_2-formation mechanism.

The decomposition process of Li_2O_2 is related to its composition and shape and was investigated using SEM, and cyclic voltammograms (CVs) during recharging. **Figure 4** clearly shows that the micrometer-sized, flower-like Li_2O_2 deposited on theRuO_2/CNT cathode surface during discharging to 2000 mAh g^{-1} (Figure 2f) immediately starts to disintegrate during recharging to 500 mAh g^{-1} (Figure 4a). Remnants of the flower-like Li_2O_2 assemblies remain visible, but many melted from the surface, which becomes rougher. Next, the Li_2O_2 assemblies decrease in size and eventually disappear

completely, as shown by the SEM images during charging to 1000 mAh g^{-1} (Figure 4b) and at full charge (Figure 4c). This is further confirmed by the PXRD and Fourier transform infrared (FTIR) measurements, which indicate that the Li_2O_2 discharge products are no longer visible (Figure 4d,e), consistent with the impedance analysis results (Figure S8, Supporting Information). Sizable Li_2O_2 products are well known to allow an appreciable discharge capacity, which agrees well with Figure 2i, but their decompositions are difficult, leading to a high charge potential. Interestingly, our experimental observations show that the charge potential of the Li–O_2 cell can be significantly improved by the RuO_2/CNT cathode (Figure 4f). Specifically, its average charge potential is much lower (by 840 mV at 200 mA g^{-1} and by 1100 mV at 500 mA g^{-1}) than that with the pristine CNT cathode (Figure 4f and Figure S9, Supporting Information). How can the promoter affect the recharge process is unknown given the large (≈9 μm in size) flower-like Li_2O_2 assemblies formed during discharge. However, we argue that the charge voltage differences may be attributable to the different Li_2O_2 decomposition mechanisms. Previous reports have theoretically and experimentally demonstrated that the decomposition of Li_2O_2 during the charge process could proceed through two different pathways[35]

$$Li_2O_2 \rightarrow Li^+ + e^- + LiO_2 \quad (4)$$

$$LiO_2 + LiO_2 \rightarrow Li_2O_2 + O_2 \quad (5)$$

or

$$Li_2O_2 \rightarrow 2Li^+ + 2e^- + O_2 \quad (6)$$

Figure 4g schematically shows the two electrochemical (or chemical) pathways for Li_2O_2 decomposition. The first pathway (two-electron transfer) is associated with the delithiation of Li_2O_2 to form LiO_2 species in the first step via a solid-solution route (Equation (4)). In the second step, the metastable LiO_2 disproportionates to evolve O_2, leading to an overall $2e^-/O_2$ oxygen evolution process (Equation (5)). The second pathway (single-electron transfer) involves the direct electrochemical decomposition of Li_2O_2 via a two-electron process (Equation (6)). The charge overpotential of the Li_2O_2 decomposition through the first pathway is lower than that through the second pathway. Based on the data presented above, we postulate that the enhanced LiO_2 solvation ability on the RuO_2/CNT cathode enables disproportionation pathways, such as Equation (5), leading to the single-electron transfer pathway that oxidizes Li_2O_2. To support this hypothesis, the electrochemical processes of oxygen in the Li–O_2 cell were also investigated using CV (Figure 4h). In the CV curves for the Li–O_2 cell with CNT cathode, only a single oxidation peak is observed at 4.25 V ($E_{a,1}$). This potential agrees well with the galvanostatic experiments (Figure 4f) and probably corresponds to the electrochemical decomposition of Li_2O_2 via a two-electron pathway (Equation (6)). Interestingly, three partially overlapping oxidation peaks for the Li–O_2 cell with RuO_2/CNT appear at lower potentials of 3.35 V ($E_{b,1}$), 3.72 V ($E_{b,2}$), and 3.90 V ($E_{b,3}$). We speculate that peak $E_{b,1}$ can be attributed to the oxidation of the superoxide-like species ($Li_{2-x}O_2$) on the surface of the flower-like Li_2O_2 assemblies through the single-electron transfer pathway

$$Li_{2-x}O_2 \rightarrow (1-x)Li^+ + (1-x)e^- + LiO_2 \quad (7)$$

This speculation is consistent with the recent conclusions of Yang et al., who reported that a superoxide-like component forms on the peroxide surface, as confirmed by low-temperature Raman spectra and magnetic measurements.[36] The oxidation of a superoxide-like component was proposed to cause this low oxidation potential.[37] Peak $E_{b,2}$ is assigned to the oxidation of the inside of the flower-like Li_2O_2 assemblies formed in the initial discharge process through the single-electron transfer pathway (Equation (4)). Peak $E_{b,3}$ is assigned to the oxidation of Li_2O_2 through the two-electron transfer pathway (Equation (6)). These results suggest that the recharge processes in the Li–O_2 cell with the RuO_2/CNT cathode are partially switched from a two-electron pathway to a single-electron one, resulting in a lower potential by improving the Li_2O_2-oxidation kinetics. We also observed that the Li_2O_2 oxidation peak $E_{b,3}$ through the two-electron transfer process of the Li–O_2 cell with RuO_2/CNT is 350 mV lower than that of the pristine CNT cathode, suggesting that the RuO_2/CNT cathode effectively improves the thermodynamics of Li_2O_2 oxidation, in agreement with previous studies. Naturally, the real recharge processes likely consist of an intricate combination of all possible pathways. More studies are needed to clarify the complex charge mechanism.

The above studies, which combined electrochemical and DFT calculation methods, confirm the superiority of the RuO_2/CNT cathode in terms of the improved kinetics and thermodynamics of Li_2O_2 formation/decomposition, which encourage us to further investigate the cycling stability of the Li–O_2 cell. The voltage obtained at the discharge terminal of the RuO_2/CNT cathode in the Li–O_2 cell is >2.0 V for 171 and 103 cycles at current densities of 200 and 500 mA g^{-1}, respectively (**Figure 5**a), which is much better than the reported results. In contrast, the discharge voltages of the CNT degrade to <2.0 V after only 45 and 10 cycles, respectively. This confirms that the RuO_2/CNT cathode has superior rechargeability and cycling stability. We extended the battery test by determining the cycling response at a specific capacity limit of 500 mAh g^{-1} and a current density of 200 mA g^{-1}. As shown in Figure S10 (Supporting Information), more than 400 stable cycles are obtained based on the RuO_2/CNT cathode, significantly outperforming the 135 stable cycles of the CNT cathode. To further understand this superior performance, the evolution of the morphology and crystallinity of the discharged cathodes after the 1st, 5th, and 20th cycles was examined. In the CNT cathode, although the discharge products at the end of the 1st discharge have a disc/toroid morphology, the discs/toroids cannot be detected after only five cycles (Figure 5b–d). In sharp contrast, in the RuO_2/CNT cathode, there is clear evidence of micrometer-sized, flower-like assemblies even after 30 cycles (Figure 5e–g and Figure S11a, Supporting Information). The crystallinity of Li_2O_2 show similar trends (Figure 5h,i and Figure S11b,d, Supporting Information). We speculate that the degradation of the morphology and crystallinity of Li_2O_2 on the pristine CNT cathode during cycling is highly possible because of the occurrence of parasitic electrochemistry (or chemistry) in the Li–O_2 cell: (1) increasing

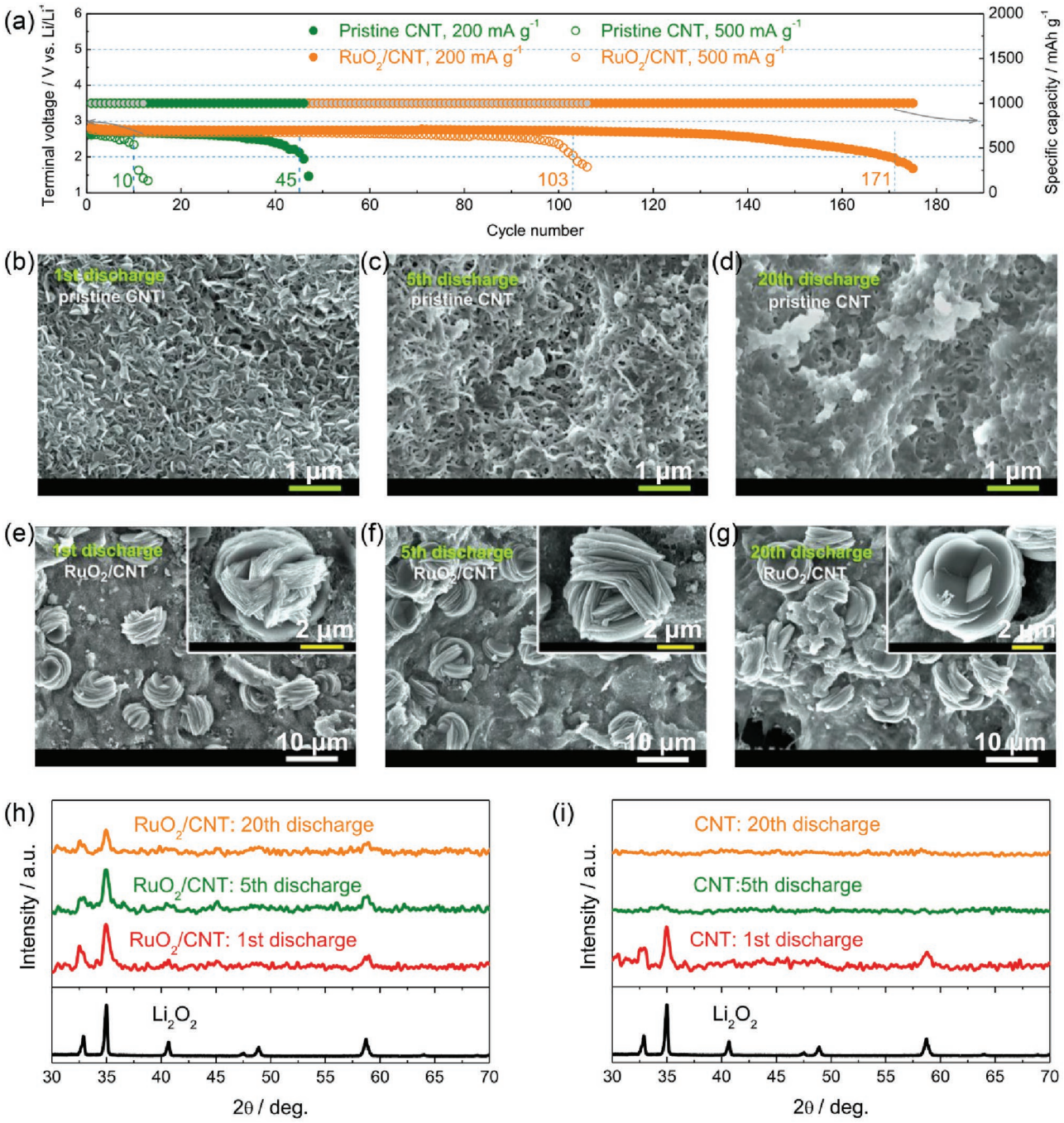

Figure 5. Product morphology and crystallinity upon cycling. a) Variation of the terminal voltage upon the discharge of the Li–O_2 cells at current densities of 200 and 500 mA g^{-1} and a specific capacity limit of 1000 mAh g^{-1}. FESEM images of b) the 1st discharged pristine CNT cathode. The current density is 200 mA g^{-1} and the specific capacity is 2000 mAh g^{-1}, c) the CNT after the 5th discharge and d) the CNT after the 20th discharge. FESEM images of e) the RuO_2/CNT cathode after the first discharge at a current density of 200 mA g^{-1} and a specific capacity of 2000 mAh g^{-1}, f) the RuO_2/CNT after the 5th discharge and g) the RuO_2/CNT after the 20th discharge. The current density is 200 mA g^{-1} and the specific capacity is 2000 mAh g^{-1}. Insets of (e–g) show the corresponding enlarged FESEM images. PXRD patterns of h) discharge products on the pristine CNT cathode and i) the RuO_2/CNT cathode at the end of discharge after the indicated number of cycles. The patterns for Li_2O_2 are also shown for reference.

accumulation of the side products (Li_2CO_3 and lithium carboxylates) on the cathode surface and (2) the presence of CO_2 in the electrolyte from the electrochemical oxidation of the side products during charging, inhibiting the nucleation and growth of Li_2O_2 during the subsequent discharge (vide infra). To this end, the parasitic electrochemistry/chemistry in the Li–O_2 cells was examined by quantitative FTIR and ^{1}H nuclear magnetic resonance (NMR) spectroscopy. The FTIR spectra indicate that the products in Li–O_2 cells with both pristine CNT and RuO_2/CNT cathodes after the first discharge are overwhelmingly dominated

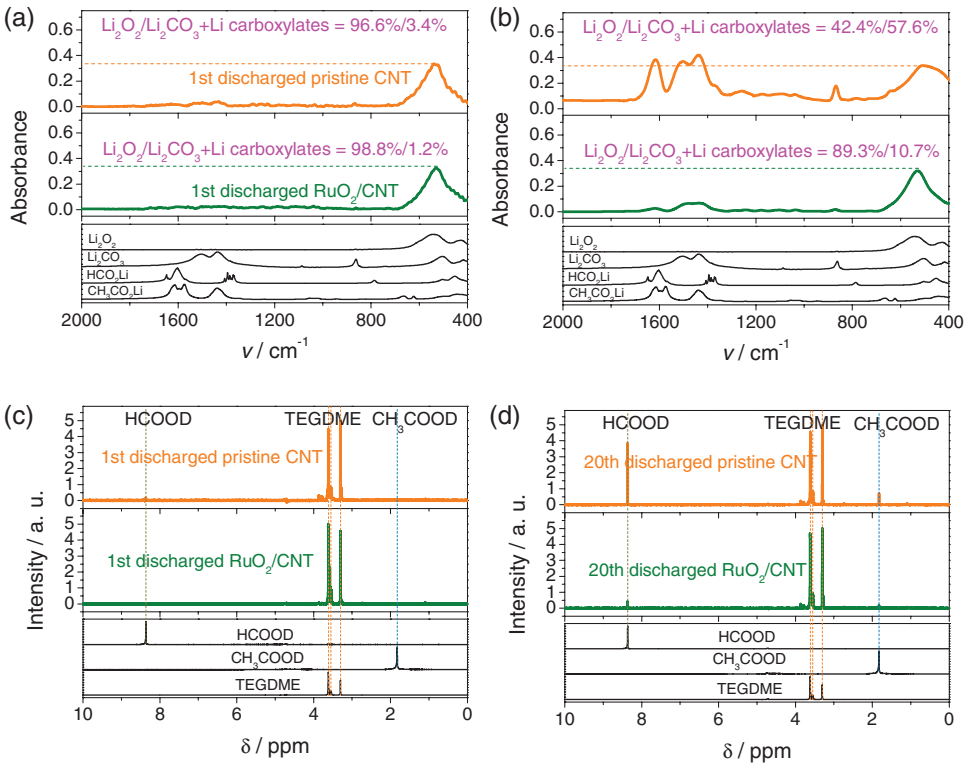

Figure 6. FTIR spectra of the pristine CNT and RuO_2/CNT cathodes after a) the 1st discharge and b) the 20th discharge. The spectra for Li_2O_2, Li_2CO_3, HCO_2Li, and CH_3CO_2Li are also shown for reference. ^1H NMR spectra of the pristine CNT and RuO_2/CNT cathodes after c) the 1st discharge and d) the 20th discharge. The spectra for TEGDME(tetraethylene glycol dimethyl ether), HCO_2Li, and CH_3CO_2Li are also shown for reference.

by Li_2O_2 (**Figure 6**a), which is in accordance with the PXRD data (Figure 2h). However, after the 20th cycle, FTIR provides clear evidence of significant side reactions on the pristine CNT cathode at the end of discharge. In addition to Li_2O_2, the peaks at ≈864, 1441, and 1500 cm^{-1} can be assigned to Li_2CO_3, that at ≈1371 cm^{-1} to HCO_2Li, and that at ≈1615 cm^{-1} to CH_3CO_2Li (Figure 6b). In contrast, significantly weaker peaks are ascribed to side products on the RuO_2/CNT cathode after 20 discharges (Figure 6b) and may have resulted from the partial decomposition of the ether-based electrolyte. Based on FTIR calibration curves obtained in our recent work,[34,38] the molar ratio of the Li_2O_2 to the side products (Li_2CO_3, CH_3CO_2Li, and HCO_2Li) was determined using the obtained FTIR spectra (Figure 6). In sharp contrast, the molar Li_2O_2/side product ratio at the end of 20 cycles for the Li–O_2 cell with the pristine CNT was only 42.4/57.6, which is much lower than that obtained with the RuO_2/CNTcathode (89.3/10.7). In addition, ^1H NMR spectroscopy (Figure 6c,d and Figure S12, Supporting Information) indicates that the amount of electrolyte decomposition products (CH_3CO_2Li and HCO_2Li) on the RuO_2/CNT cathode is much less than that on the pristine CNT cathode during cycling, which is consistent with the above FTIR results. These observations clearly demonstrate the superiority of the Li–O_2 cells with the RuO_2/CNT cathode in terms of the electrochemical/chemical stability, which can be ascribed to the ability of the RuO_2 protective layer on the CNT to effectively prevent direct contact between the CNT defect sites and the Li_2O_2 or between the defect sites and electrolyte and, thus, effectively prevent or reduce the possible side reactions. In addition, the low charge potential observed with the RuO_2/CNT cathode alleviates the high-potential-induced decomposition of the electrolyte and carbon cathode during charging, which also contributes to the high electrochemical/chemical stability. The effect of parasitic electrochemistry/chemistry on the evolution of the morphology and crystallinity of Li_2O_2 is discussed in detail (see Figure S15, Supporting Information).

Our work establishes a new growth, decomposition, and evolution mechanisms of Li_2O_2 upon cycling in Li–O_2 cells using a highly stable cathode based on CNTs coated with RuO_2. The RuO_2/CNT cathode possessing a feeble surface binding energy toward the superoxide species (as LiO_2, O_2^-) to promote the formation of LiO_2, with O_2^- readily diffusing to the electrolyte, is biased to enhance both the solvation-mediated growth of Li_2O_2 during discharging and the single-electron transfer oxidation of Li_2O_2 during recharging, leading to efficient formation/decomposition of the micrometer-sized, flower-like Li_2O_2 assemblies reported here for the first time. We also demonstrate that the rapid formation/decomposition mechanism of the micrometer-sized, flower-like Li_2O_2 is sustainable over many cycles because of the minimal accumulation of side products on the RuO_2/CNT cathode and the presence of CO_2 in the electrolyte produced by parasitic electrochemistry/chemistry during Li–O_2 cell cycling. These advantages of the RuO_2/CNT cathode endow the Li–O_2 battery with an ultrahigh specific capacity (29 900 mAh g^{-1} and 8930 mAh g^{-1} at current densities of 200 mA g^{-1} and 2 A g^{-1}, respectively), relatively low

overpotentials (0.45 V at a current density of 200 mA g^{-1}), and a long cycle life (171 cycles at a current density of 200 mA g^{-1} and a specific capacity limit of 1000 mAh g^{-1}). Hence, we believe that the results presented here will encourage further studies of the electrochemical mechanism of Li–O_2 batteries, although many challenges remain to be overcome before practical devices can be realized.

Supporting Information

Supporting Information is available from the Wiley Online Library or from the author.

Acknowledgements

J.-J.X., Z.-W.C., and Y.W. contributed equally to this work. This work was financially supported by National Program on Key Basic Research Project of China (2012CB215500 and 2014CB932300), Strategic Priority Research Program of the Chinese Academy of Sciences (Grant No. XDA09010404), and National Natural Science Foundation of China (21422108, 21271168, and 51472232).
Note: The acknowledgements were updated on November 10, 2016, after initial publication online.

Received: June 30, 2016
Revised: July 26, 2016
Published online: September 16, 2016

[1] P. G. Bruce, S. A. Freunberger, L. J. Hardwick, J. M. Tarascon, *Nat. Mater.* **2012**, *11*, 19.
[2] T. Liu, M. Leskes, W. Yu, A. J. Moore, L. Zhou, P. M. Bayley, G. Kim, C. P. Grey, *Science* **2015**, *35*, 530.
[3] S. H. Oh, R. Black, E. Pomerantseva, J. H. Lee, L. F. Nazar, *Nat. Chem.* **2012**, *4*, 1004.
[4] J. Lu, Y. J. Lee, X. Luo, K. C. Lau, M. Asadi, H.-H. Wang, S. Brombosz, J. Wen, D. Zhai, Z. Chen, D. J. Miller, Y. S. Jeong, J.-B. Park, Z. Z. Fang, B. Kumar, A. S-Khojin, Y.-K. Sun, L. A. Curtiss, K. Amine, *Nature* **2016**, *529*, 377.
[5] J. Zhu, F. Wang, B. Wang, Y. Wang, J. Liu, W. Zhang, Z. Wen, *J. Am. Chem. Soc.* **2015**, *137*, 13572.
[6] Q.-C. Liu, J.-J. Xu, S. Yuan, Z. W. Chang, D. Xu, Y.-B. Yin, L. Li, H.-X. Zhong, Y.-S. Jiang, J.-M. Yan, X.-B. Zhang, *Adv. Mater.* **2015**, *27*, 5241.
[7] K. M. Abraham, Z. Jiang, *J. Electrochem. Soc.* **1996**, *143*, 1.
[8] Z. Peng, S. Freunberger, Y. Chen, P. G. Bruce, *Science* **2012**, *337*, 563.
[9] M. M. O. Thotiyl, S. A. Freunberger, P. Zhuangquan, C. Yuhui, L. Zheng, P. G. Bruce, *Nat. Mater.* **2013**, *12*, 1050.
[10] T. Ogasawara, A. Débart, M. Holzapfel, P. Novák, P. G. Bruce, *J. Am. Chem. Soc.* **2006**, *128*, 1390.
[11] B. D. McCloskey, A. Valery, A. C. Luntz, S. R. Gowda, G. M. Wallraff, J. M. Garcia, T. Mori, L. E. Krupp, *J. Phys. Chem. Lett.* **2013**, *4*, 2989.
[12] S. A. Freunberger, Y. Chen, N. E. Drewett, L. J. Hardwick, F. Barde, P. G. Bruce, *Angew. Chem. Int. Ed.* **2011**, *50*, 8609.
[13] Y. Shao, F. Ding, J. Xiao, J. Zhang, W. Xu, S. Park, J.-G. Zhang, Y. Wang, J. Liu, *Adv. Funct. Mater.* **2013**, *23*, 987.
[14] T. Zhang, H. Zhou, *Angew. Chem. Int. Ed.* **2012**, *51*, 11062.
[15] S. Lau, L. A. Archer, *Nano Lett.* **2015**, *15*, 5995.
[16] Y. S. Mekonnen, J. M. Garcia-Lastra, J. S. Hummelshøj, C. Jin, T. Vegge, *J. Phys. Chem. C* **2015**, *119*, 18066.
[17] C. Xia, M. Waletzko, L. Chen, K. Peppler, P. J. Klar, J. Janek, *ACS Appl. Mater. Interfaces* **2014**, *6*, 12083.
[18] B. D. McCloskey, R. Scheffler, A. Speidel, G. Girishkumar, A. C. Luntz, *J. Phys. Chem. C* **2012**, *116*, 23897.
[19] V. Viswanathan, J. K. Nørskov, A. Speidel, R. Scheffler, S. Gowda, A. C. Luntz, *J. Phys. Chem. Lett.* **2013**, *4*, 556.
[20] J. Lu, Y. Lei, K. C. Lau, X. Luo, P. Du, J. Wen, R. S. Assary, U. Das, D. J. Miller, J. W. Elam, H. M. Albishri, D. A. Ei-Hady, Y.-K. Sun, L. A. Curtiss, K. Amine, *Nat. Commun.* **2013**, *4*, 2383.
[21] C. J. Allen, J. Hwang, R. Kautz, S. Mukerjee, E. J. Plichta, M. A. Hendrickson, K. M. Abraham, *J. Phys. Chem. C* **2012**, *116*, 20755.
[22] M. J. Trahan, S. Mukerjee, E. J. Plichta, M. A. Hendrickson, K. M. Abraham, *J. Electrochem. Soc.* **2003**, *160*, A259.
[23] N. B. Aetukuri, B. D. McCloskey, J. M. Garcia, L. E. Krupp, V. Viswanathan, A. C. Luntz, *Nat. Chem.* **2015**, *7*, 50.
[24] L. Johnson, C. Li, Z. Liu, Y. Chen, S. A. Freunberger, P. C. Ashok, B. B. Praveen, K. Dholakia, J.-M. Tarascon, P. G. Bruce, *Nat. Chem.* **2014**, *6*, 1091.
[25] B. D. Adamset, C. Radtke, R. Black, M. L. Trudeau, K. Zaghib, L. F. Nazar, *Energy Environ. Sci.* **2013**, *6*, 1772.
[26] R. R. Mitchell, B. M. Gallant, Y. Shao-Horn, C. V. Thompson, *J. Phys. Chem. Lett.* **2013**, *4*, 1060.
[27] J. Xie, X. Yao, Q. Chen, I. P. Madden, P. Dornath, C.-C. Chang, W. Fan, D. Wang, *Angew. Chem. Int. Ed.* **2015**, *127*, 4373.
[28] Z. Jian, P. Liu, F. Li, P. He, X. Guo, M. Chen, H. Zhou, *Angew. Chem. Int. Ed.* **2013**, *53*, 442.
[29] D. Zhai, H. H. Wang, J. Yang, K. C. Lau, K. Li, K. Amine, L. A. Curtiss, *J. Am. Chem. Soc.* **2013**, *135*, 15364.
[30] R. Black, B. Adams, L. F. Nazar, *Adv. Energy Mater.* **2012**, *2*, 801.
[31] J.-J. Xu, D. Xu, Z.-L. Wang, H.-G. Wang, L.-L. Zhang, X.-B. Zhang, *Angew. Chem. Int. Ed.* **2013**, *52*, 3887.
[32] Y. T. Kim, T. Mitani, *Appl. Phys. Lett.* **2006**, *89*, 033107.
[33] Q.-C. Liu, J.-J. Xu, D. Xu, X-B. Zhang, *Nat. Commun.* **2015**, *6*, 7892.
[34] J.-J. Xu, Z.-L. Wang, D. Xu, L.-L. Zhang, X.-B. Zhang, *Nat. Commun.* **2013**, *4*, 2438.
[35] S. Ganapathy, B. D. Adams, G. Stenou, M. S. Anastasaki, K. Goubitz, X.-F. Miao, L. F. Nazar, M. Wagemaker, *J. Am. Chem. Soc.* **2014**, *136*, 16335.
[36] J. B. Yang, D. Zhai, H.-H. Wang, K. C. Lau, J. A. Schlueter, P. Du, D. J. Myers, Y.-K. Sun, L. A. Curtiss, K. Amine, *Phys. Chem. Chem. Phys.* **2013**, *15*, 3764.
[37] D. Y. Zhai, H.-H. Wang, J. Yang, K. C. Lau, K. Li, K. Amine, L. A. Curtiss, *J. Am. Chem. Soc.* **2013**, *135*, 15364.
[38] J.-J. Xu, Z.-L. Wang, D. Xu, F.-Z. Meng, X.-B. Zhang, *Energy Environ. Sci.* **2014**, *7*, 2213.